A Journal of the Gesellschaft Deutscher Chemiker

Angewandte International Edition GDCh Chemie

www.angewandte.org

Accepted Article

Title: A Dual-Atom La2 Catalyst for the Oxygen Reduction Reaction

Authors: Jingru Sun, Tianmi Tang, Siying Zhang, Siyu Chen, Yingying Duan, Xue Bai, Xiaoqin Xu, Xiaodi Niu, Zhenlu Wang, and Jingqi Guan

To be cited as: *Angew. Chem. Int. Ed.* **2025**, e202509063

Link to VoR: https://doi.org/10.1002/anie.202509063

WILEY VCH

10.1002/anie.202509063

RESEARCH ARTICLE

WILEY VCH

A Dual-Atom La_2 Catalyst for the Oxygen Reduction Reaction

Jingru Sun[a], Tianmi Tang[a], Siying Zhang[a], Siyu Chen[a], Yingying Duan[a], Xue Bai[a], Xiaoqin Xu[a], Xiaodi Niu*[b], Zhenlu Wang*[a] and Jingqi Guan*[a]

[a] J. Sun, T. Tang, S. Zhang, S. Chen, Y. Duan, X. Bai, X. Xu, Z. Wang*, J. Guan*
Institute of Physical Chemistry
College of Chemistry, Jilin University
2519 Jiefang Road, Changchun 130021, P. R. China
E-mail: wzl@jlu.edu.cn, guanjq@jlu.edu.cn

[b] X. Niu*
College of Food Science and Engineering
Jilin University
Changchun 130062, China
E-mail: niuxd@jlu.edu.cn

Supporting information for this article is given via a link at the end of the document.

Abstract: Rare earth lanthanum element has large atomic radius, multi-shell orbital electrons, and Fenton-like reaction inertia, on which a localized high-coordination structure can be easily formed for the favorable adsorption of reaction intermediates. However, for single-atom lanthanum sites, due to the loss of all the outmost *s* and *d* electrons, the practically vacuous outmost orbitals are stable but sleepy for the oxygen reduction reaction (ORR). Here, we synthesize a novel dual-atom La catalyst onto N-doped graphene (La_2-NG) by a Joule ultrafast heating method, which shows a half-wave potential of 0.893 V for the ORR. The La_2-NG-assembled zinc-air battery demonstrates a great open circuit voltage of 1.52 V and a maximal power density of 192 mW cm^{-2}. Operando X-ray absorption spectra reveal the change of valence states of La and the dynamic structural evolution of La_2-N_6 moiety embedded onto the graphene during the ORR, through which the adsorption/desorption of oxygen reduction intermediates can be reasonably regulated. Theoretical calculations further demonstrate that the La_2-N_6 structure can decrease the reaction energy barrier and promote charge transfer.

Introduction

The clipping growth of population and excessive consumption of energy promote the development of energy storage and conversion devices.[1] Zinc-air batteries (ZABs) are deemed as among the most attractive candidates because of their good sustainability, portability, economic feasibility and high energy density. The ORR of cathode is the key factor that restricts the efficiency of ZABs.[2] Because of the complex reaction process and slow ORR kinetics, it is very important to develop low-cost and high-performance ORR electrocatalysts. Although noble metal electrocatalysts perform well in ORR, their high cost, poor durability, scarce resources and susceptibility to CO and methanol poisoning limit their large-scale application.[3] Therefore, it is important to design high-performance non-noble metal ORR electrocatalysts.

Recently, single-atom catalysts (SACs) have been widely studied because of their ultra-high atomic utilization, tunable electronic structure and strong resistance to acidic/alkaline media. Especially, SACs with M-N-C composition have shown remarkable ORR activity and selectivity, high stability and excellent recoverability.[4] Therefore, M-N-C SACs are considered to be the most viable materials to displace noble metal catalysts. M-N-C SACs show characteristic electronic structures different from metals or metal compounds, and the central metal atoms are in a low coordination environment, which can maximize the utilization.[5] However, SACs have some limitations. The density of active sites of SACs is low, and there are not enough adsorption sites to adsorb different reaction intermediates at the same time.[6] Moreover, they lack structural complexity, and it is challenging to control the distribution of metal atoms, which leads to the lack of synergy between catalytic sites and cannot effectively drive multi-electron and multi-proton transfer processes. Therefore, the further development of electrocatalysts with multi-atomic centers is necessary.

As an expansion of SACs, dual-atom catalysts (DACs) not only have the advantages of SACs, but also have more flexible active sites and higher metal content.[7] Therefore, DACs have superior electrocatalytic performance and long-term stability, which has attracted wide attention in the electrocatalytic filed. In addition, the synergistic effect of metal dimers in DACs leads to the characteristic electronic structure different from the corresponding single atom, thus effectively improving the catalytic ORR performance.[8] Recently, N-coordinated dual-metal-atom catalysts have significantly greater ORR performance than M-N-C SACs because of the cooperative interactions between neighboring metal centers. For example, Wang et al. designed Fe-Se diatomic sites loaded on N-doped carbon (Fe-Se/NC),[9] which showed higher ORR performance than iron-based SACs. The doping of Se can adjust the electronic configuration of Fe sites through *p-d* orbital hybridization, which effectively regulates the adsorption/desorption behavior of oxygen reduction intermediates. Jiang et al. developed a dual-atom Fe catalyst supported on N-doped carbon (Fe-N-HCS-900) by implanting Fe_2N_5 sites into hollow carbon spheres.[10] Fe-N-HCS-900 has better ORR performance and long-term stability than Fe-N-C. In addition, DACs such as Fe-Co,[11] Fe-Cu,[12] Fe-Mn,[13] Co-Pt[14] and Cu-Zn[15] all show high ORR activity and four-electron

transfer route. Obviously, bimetallic sites enrich the diversity of metal centers of ORR catalysts. However, Fe-/Co-based DACs are unstable during longstanding ORR, which are susceptible to the attack of peroxide-derived reactive oxygen species, leading to the degradation and inactivation. Therefore, to further improve the ORR stability, it is necessary to reasonably introduce dual-metal sites with Fenton-like reaction sluggishness.

Because of the special 4f shell electronic configuration, rare earth elements introduce tunable electronic properties and pronounced spin-orbit coupling to coupled d band centers, improving electrocatalytic performance.[16] Mixed valence of rare earth metal can enhance redox performance, thus enhancing ORR activity. In recent years, rare earth metal oxides have been applied to ORR because of their distinctive 4*f* electronic configurations and effective active centers. Ghosh et al. synthesized CeO_2 hollow spheres by a solvothermal method, which showed excellent ORR catalytic activity, four-electron selectivity, methanol tolerance and stability.[8c] Zhao et al. deposited hexagonal La_2O_3 nanocrystals on nitrogen-rich porous carbon to obtain La_2O_3/NPC catalyst.[17] La_2O_3/NPC hybrid showed excellent ORR activity, stability and methanol tolerance under alkaline conditions. In addition, like transition metals, rare earth metals also have the potential to form M-N-C active sites, which can enhance the activity of electrocatalysts.[18] Zhao et al. synthesized Ce SACs catalysts (CeNCs) to improve neutral ORR.[19] In neutral media, CeNC-40 exhibited high ORR activity with a half-wave potential ($E_{1/2}$) of 0.78 V, and the activity attenuation can be ignored after 10000 potential cycles. However, up to now, there is no report about rare earth metal DACs in ORR electrocatalysis.

Here, we anchored dual-atom La_2 on N-doped graphene by Joule ultrafast heating method to obtain a novel La_2-NG DAC. In 0.1 M KOH, La_2-NG exhibited higher ORR activity ($E_{1/2}$ = 0.893 V than La_1-NG SAC and commercial Pt/C catalysts. In addition, the La_2-NG-assembled ZAB showed a high specific capacity (805 mAh g_{Zn}^{-1}), a power density of 192 mW cm^{-2}, high charge-discharge efficiency, and good stability. DFT calculations revealed that La_2-N_6 configuration shows lower ORR barrier than La_2-C_x, La_2-N_2O_4, and La_2-O_6, implying La_2-N_6C_x as the active site. Operando X-ray absorption spectra (XAS) revealed that La_2-NG experienced a dynamic structural evolution during the ORR process.

Results and Discussion

Synthesis and Characterization

Figure 1a shows the synthesis process of La_2-NG. The dual-atom La_2 sites from $[La_2(BA)_4(NO_3)_2(phen)_2]$ precursor (Figures S1 and S2) were embedded onto the N-doped graphene by flash pyrolysis on a Joule ultrafast heating device.[20] Through precise control of the metal concentration and pyrolysis temperature, x-La_2-NG-T catalysts with different La loadings (x = 0.3 ~ 1 wt.%) and pyrolysis temperatures (T = 1100 ~ 1700 ℃) were synthesized. For simplicity, the optimal catalyst, 0.5%-La_2-NG-1500, is hereafter referred as La_2-NG. For comparison, an N-free dual-atom La catalyst (La_2-G) and a single-atom La catalyst (La_1-NG) were also prepared using an analogous approach. The morphology and element distribution of La_2-NG were respectively analyzed by transmission electron microscope (TEM), high-resolution TEM (HRTEM) and energy dispersive spectrometer (EDS). As shown in Figure 1b, c, the TEM and HRTEM images of La_2-NG show a folded nanosheet structure and no metal nanoparticles or clusters. The elemental maps clearly display that La and N exist in the La_2-NG catalyst and are evenly distributed on the whole graphene nanosheets (Figure 1d). The dual-atom La_2 sites dispersed on N-doped graphene were confirmed via high-angle annular dark-field scanning transmission electron microscope (HAADF-STEM), illustrating a large number of adjacent bright spots (marked with red squares) (Figure 1e, f), indicating the formation of metal La dimers. Additionally, the distance between two La atoms in the dimers is ca. 0.34 nm, indicating the formation of a stable coupled La diatomic structure (Figure 1g, h).

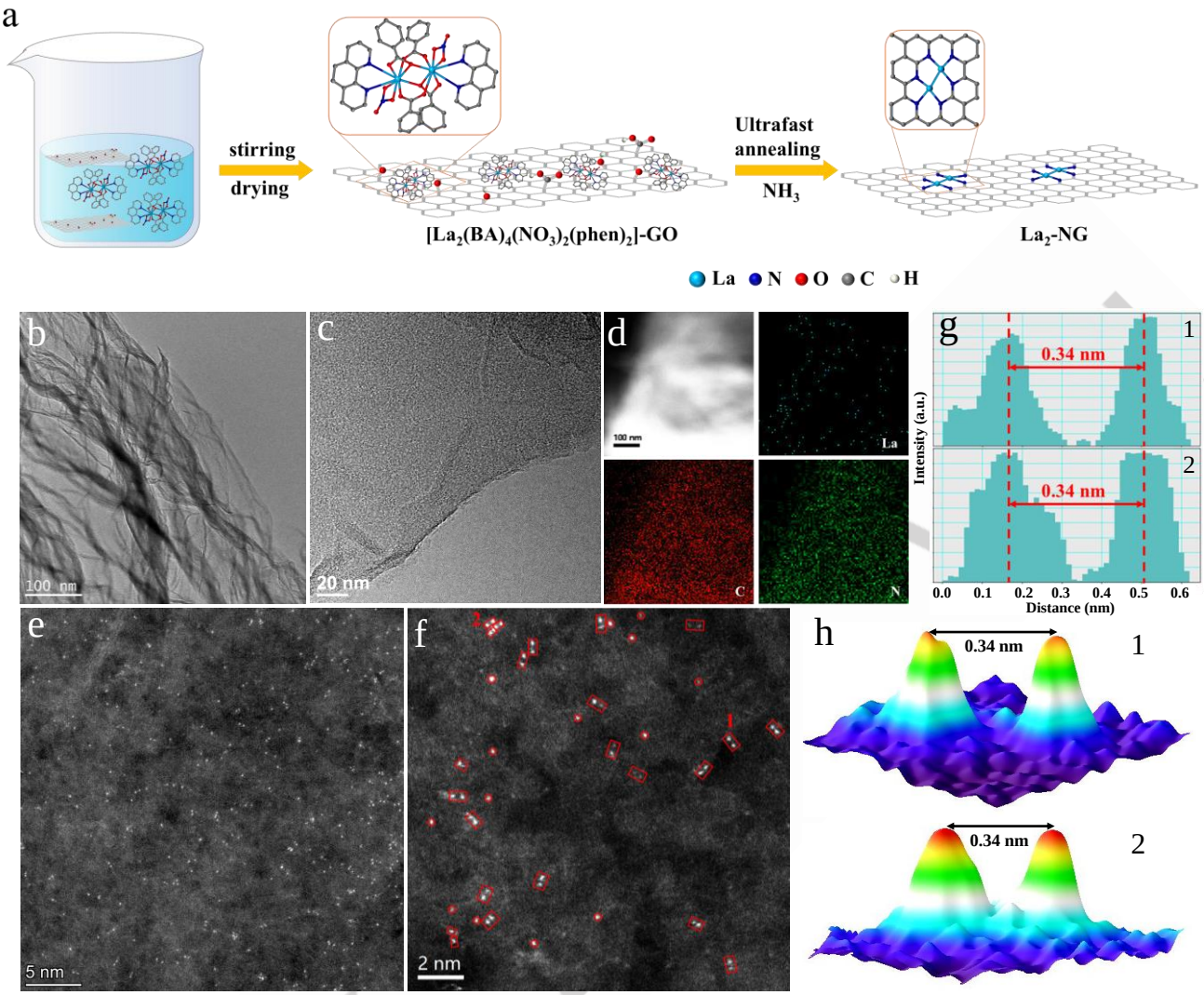

Figure 1. (a) Synthetic illustration, (b) TEM image, (c) HRTEM image, (d) element mapping, and (e, f) HAADF-STEM images of La_2-NG. (g) Intensity distribution and (h) 3D model of the atomic sites in (f).

The crystal structures of La_2-NG and La_1-NG were studied by X-ray diffraction (XRD). From Figure 2a, two peaks are observed at about 25° and 44°, corresponding to the graphite lattice planes.[21] Notably, no peaks of La nanoparticles and La oxides or carbides are observed, confirming that the metal species are atomically dispersed on graphene-based carriers. The surface elemental distribution and oxidation state of La were evaluated by X-ray photoelectron spectroscopy (XPS). The XPS survey spectrum of La_2-NG indicates the main existence of C, O, and N elements (Figure S3). The La 3d XPS spectrum is fitted into four characteristic peaks (Figure 2b). The characteristic peaks at 834.1 and 841.7 eV correspond to La $3d_{5/2}$, and the characteristic peaks at 853.1 and 861.2 eV correspond to La $3d_{3/2}$, confirming that the valence state of La is close to +3.[22] The deconvoluted N 1s spectra reveals five peaks (Figure 2c), corresponding to pyridinic-N (398.4 eV), La-N (399.0 eV), pyrrolic-N (400.2 eV), graphitic-N (401.2 eV) and oxidized-N (404.0 eV).[23]

To elucidate the electronic configuration and atomic coordination of La_2-NG, X-ray absorption near-edge structure (XANES) and extended X-ray absorption fine structure (EXAFS) analyses were carried out. As shown in Figure 2d, the La L-edge XANES spectra of La_2-NG, La_1-NG and La_2O_3 show that the white line intensity of La_2-NG is located between La_1-NG and La_2O_3, demonstrating that the La in La_2-NG is positively charged with an oxidation state lower than +3 but higher than that in La_1-NG. The EXAFS spectra of La_2-NG, La_1-NG and La_2O_3 are shown in Figure 2e, displaying significant difference. The La_2-NG displays La-N/O path in the first shell and La-La path in the second shell, while the La_1-NG displays only La-N/O path and no La-La path, meaning that the La atoms in the La_1-NG are atomically dispersed, while they are dimers in the La_2-NG in consistence with the aforementioned HAADF-STEM result. The fitting Fourier transform (FT)-EXAFS spectrum of La_2-NG indicates that one La atom in the La_2-NG is coordinated with 3 N and 1 La atoms with La-N bond length of 2.48 Å and La-La bond length of 3.40 Å (Figure 2f and Table S1). Thus, the simulated structure is displayed in Figure 2g, indicating LaN_3–LaN_3 atomic pair configuration, while the main sites in La_1-NG are LaN_4 (Figure S4 and Table S1). The wavelet transform (WT) EXAFS spectrum of La_2-NG exhibits a prominent signal at (1.93 Å，4.99 $Å^{-1}$), corresponding to La-N coordination.[24] Moreover, a second

intensity maximum at (2.65 Å，4.85 $Å^{-1}$), corresponds to La-La coordination, confirming the existence of La DAs (Figure 2h). WT-EXAFS analysis of La_1-NG exhibits only one contour intensity maxima at ~1.87 $Å^{-1}$ in k-space (Figure 2i), which is significantly different from La_2-NG and La_2O_3 (Figure 2j). The successful formation of diatomic La sites is due to the instantaneous decomposition of the binuclear La complex precursor, while ammonia pyrolysis generates reactive nitrogen species that subsequently form La-N bonds.[25] Single-atom La species might be generated by the decomposition of some unstable La dimers.

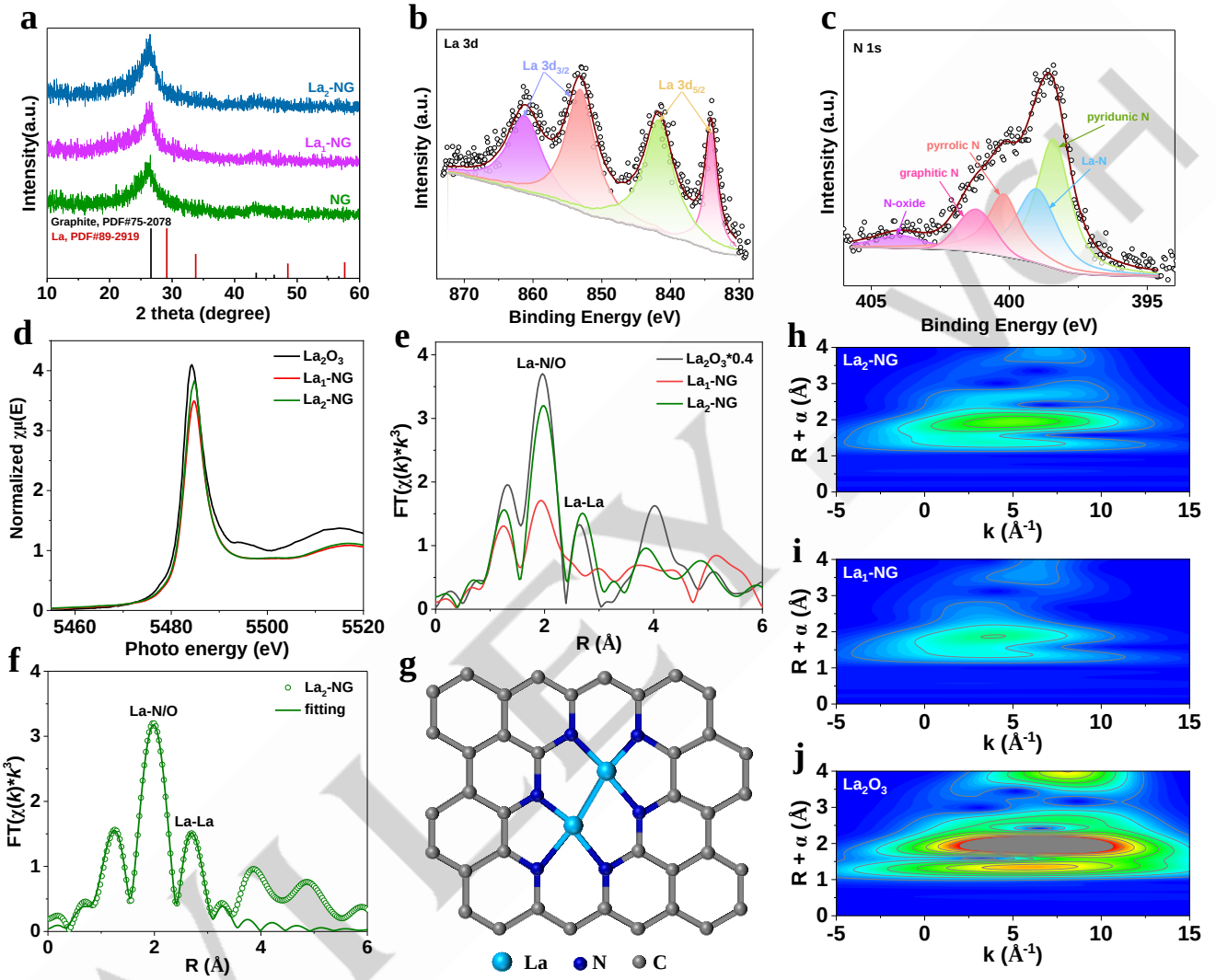

Figure 2. (a) XRD patterns. (b) La 3d and (c) N 1s XPS spectra of La_2-NG. (d) La L-edge XANES spectra of La_2-NG and referred samples La_1-NG and La_2O_3. (e) k^3-weighted EXAFS spectra of La_2-NG、La_1-NG and La_2O_3. (f) Experiment and FT-EXAFS fitting curves of La L-edge of La_2-NG in R space. (g) The simulated structure. WT-EXAFS spectra of (h) La_2-NG, (i) La_1-NG, and (j) La_2O_3.

ORR Performance

The electrochemical ORR performance was appraised in O_2-saturated 0.1 M KOH. The cyclic voltammogram (CV) curves demonstrate that a more positive cathode peak is observed for the La_2-NG than the control samples graphene (G), N-doped graphene (NG), La_1-NG, La_2-G, and Pt/C, meaning greater ORR activity of the La_2-NG (Figure 3a). Furthermore, the ORR activity of La_2-NG was further evaluated by linear sweep voltammetry (LSV) curves. From Figure 3b, La_2-NG shows a positive initial potential (E_{onset}) of 0.973 V and $E_{1/2}$ of 0.893 V, which are higher than those of Pt/C (E_{onset} = 0.895 V and $E_{1/2}$ = 0.823 V), G (E_{onset} = 0.812 V and $E_{1/2}$ = 0.737 V), NG (E_{onset} = 0.857 V and $E_{1/2}$ = 0.743 V), La_2-G (E_{onset} = 0.802 V and $E_{1/2}$ = 0.726 V) and La_1-NG (E_{onset} = 0.861 V and $E_{1/2}$ = 0.743 V), further illustrating that La_2-NG shows the best catalytic ORR activity among these samples. The diffusion-limited current density of La_2-NG at 0.4 V is −5.93 mA cm^{-2}, which exceeds Pt/C (−5.44 mA cm^{-2}), G (−1.53 mA cm^{-2}), NG (−2.12 mA cm^{-2}), La_2-G (−3.43 mA cm^{-2}) and La_1-NG (−4.23 mA cm^{-2}), meaning its excellent mass transfer performance and inherent catalytic activity.[26] The catalytic kinetics was investigated by Tafel slope.[27] From Figure 3c, the

Tafel slope of La_2-NG is 39 mV·dec^{-1}, which is lower than that of Pt/C (56 mV dec^{-1}), G (113 mV dec^{-1}), NG (102 mV dec^{-1}), La_2-G (63 mV dec^{-1}) and La_1-NG (76 mV dec^{-1}), meaning that the La_2-NG catalyst exhibits the optimum ORR kinetics. Furthermore, the electrocatalytic active sites were estimated by double-layer capacitance (C_{dl}) and electrochemical active surface area (ECSA) of the catalysts (Figure 3d and Figures S5-S10). The values of C_{dl} and ECSA of La_2-NG are calculated to be 15.90 mF cm^{-2} and 407 cm^2, which are higher than those of G (4.94 mF cm^{-2}, 124.6 cm^2), NG (10.40 mF cm^{-2}, 262 cm^2), La_2-G (7.27 mF cm^{-2}, 183.6 cm^2), La_1-NG (13.65 mF cm^{-2}, 338.8 cm^2) and Pt/C (15.49 mF cm^{-2}, 395.3 cm^2), demonstrating that La_2-NG provides more electroactive sites for the ORR. The influence of synthesis temperature (Figure S11) and La content (Figure S12) on catalytic ORR performance was studied, demonstrating that the synthesis temperature of 1500 ℃ and 0.5 wt.% La content is the best. The results indicate that optimal La doping content and annealing temperatures maximize the formation of La_2-N_6 active sites, achieving high density of active sites and favorable charge transfer.[28] It is observed that the ORR activity of La_2-NG exceeds most dual-atom ORR electrocatalysts reported previously (Figure 3e and Table S2).

The electron transfer number (n) determines the ORR pathway, which can be evaluated through the derived Koutecky–Levich (K-L) plot. The diffusion current density of La_2-NG is gradually increased with rotation rate elevation from 400 rpm to 2500 rpm (Figure 3f). The K-L diagram shows that n is about 3.97 (the inset in Figure 3f), indicating that La_2-NG exhibits preferential 4e$^-$ ORR activity. Subsequently, the rotating ring disk electrode (RRDE) test was conducted to evaluate the yield of H_2O_2 and n value (Figure S13 and Figure 3g). The H_2O_2 yield on the La_2-NG is less than 6% and the average n value is 3.92, further indicating a dominant four-electron pathway and ultra-high selectivity of oxygen reduction to H_2O. To evaluate the practical feasibility of the La_2-NG, the stability and methanol resistance were tested by chronoamperometry (Figure 3h). Compared with the initial state, La_2-NG shows only 7.4% current degradation in the continuous 12 h test, while the current degradation of Pt/C is as much as 42.3%. In addition, after 200 s of chronoamperometric measurement, the methanol resistance test was performed after adding 3 M methanol (Figure 3i). Commercial Pt/C exhibits obvious current drop after adding methanol, while La_2-NG maintains a relatively stable current response after adding methanol, indicating the strong resistance to methanol poisoning.

The main active sites of ORR were explored by KSCN poisoning test. After introducing 10 mM KSCN into 0.1 M KOH solution (Figure S14), similar to Pt/C catalyst, the E_{onset}, $E_{1/2}$ and limiting current density of La_2-G, La_1-NG and La_2-NG all decreased greatly, indicating that the coordination between La and SCN$^-$ led to the inactivation of metal active sites. The results further confirm that La_2-N_x is the main electrocatalytic active site of La_2-NG for the ORR. To clarify the potential reaction mechanism on the La_2-NG, we used operando Raman spectroscopy to monitor the structural changes and ORR intermediates under different applied potentials (Figure S15). When the voltage changes from 1.0 to 0.2 V, a broad peak appears at around 1147 cm^{-1}, which can be corresponding to the O-O stretching peak of superoxide, proving that the first step of ORR is single electron transfer, and $*O_2$ is converted into $*O_2^-$.[29] The Raman peak at about 1550 cm^{-1} is corresponding to the O-OH stretching vibration in the *OOH intermediate, showing that $*O_2^-$ is further transformed into *OOH.[30] The structure of La_2-NG after ORR was analyzed by XRD (Figure S16), demonstrating that La-based nanoparticles were not formed. In addition, XPS was conducted to characterize the change of the chemical state of the La_2-NG after ORR (Figure S17). The binding energy of La 3d peak does not shift after ORR, indicating that the valence state of La is ~ +3. The peak representing La-N is still present after ORR, indicating the durability of the metal active sites.

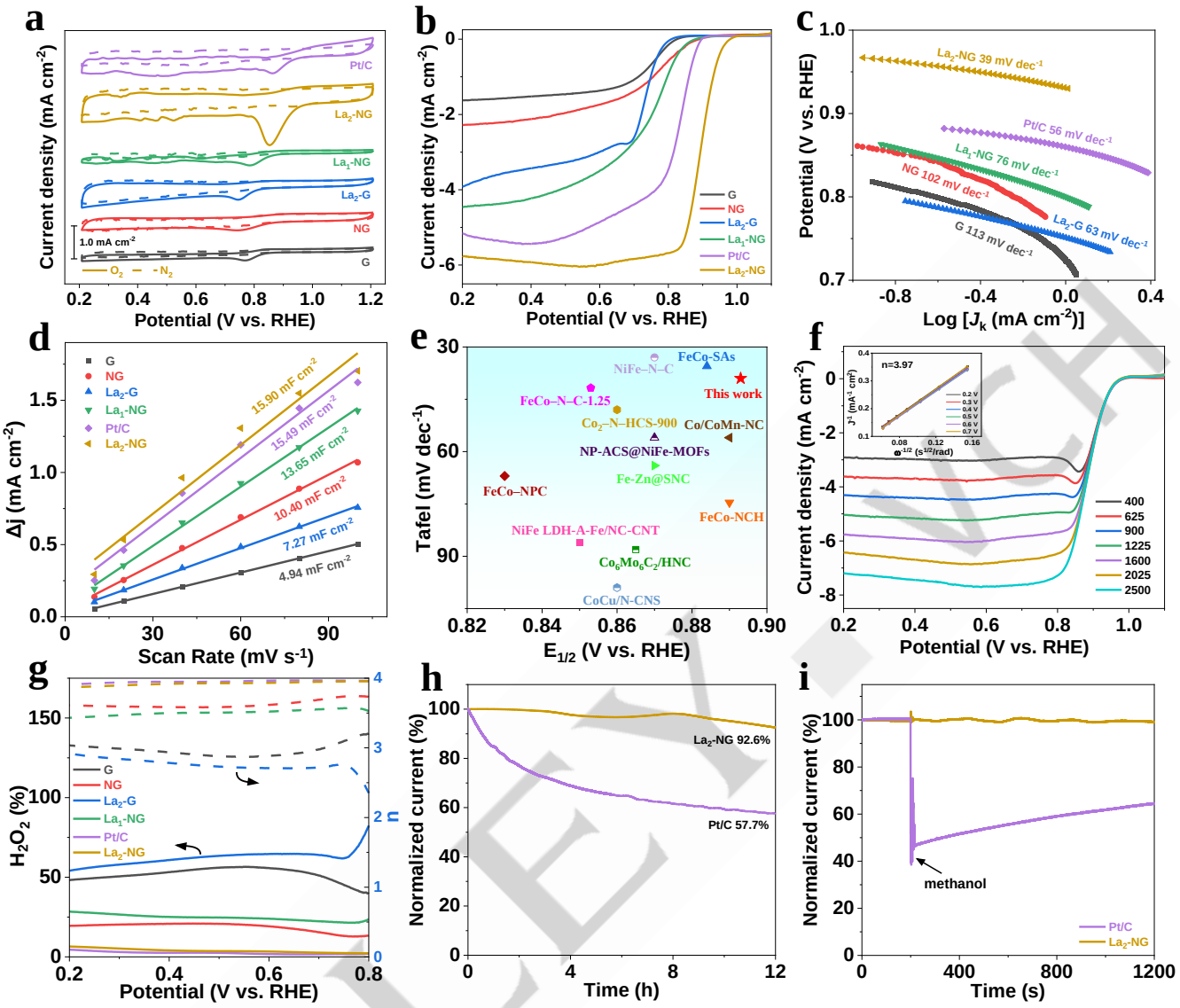

Figure 3. (a) CV curves (dashed lines: N_2; solid lines: O_2). (b) LSV curves. (c) Tafel slopes. (d) Capacitive *j* vs scan rate for G, NG, Pt/C, La_2-G, La_1-NG, and La_2-NG. (e) Comparison of $E_{1/2}$ and Tafel slope of La_2-NG with DACs reported previously. (f) LSV curves of La_2-NG at different rotation speeds and K-L plot (inset). (g) H_2O_2 yield and n. (h) Chronoamperometry tests of La_2-NG and Pt/C. (i) Chronoamperometric response of La_2-NG and Pt/C in 0.1 M KOH with 3 M methanol.

The ORR mechanism on the La_2-NG was investigated by operando XAS. Figure 4a shows XANES spectra of La_2-NG under different applied potentials. The white line intensity of La_2-NG in the potential range of 0.5 - 0.9 V is slightly lower than that at open circuit potential (OCP). Moreover, the white line intensity of XANES moves down when the potential decreases from 0.9 to 0.5 V, demonstrating that more La sites were reduced to lower oxidation states during ORR. The oxidation state of La in the La_2-NG under different potentials was calculated by using white line peak area method, exhibiting +3.07, +2.87, +2.80, and +2.78 for OCP, 0.9 V, 0.7 V and 0.5 V, respectively (Figure S18). This reduction weakens OH adsorption on La sites, promoting OH^- desorption and consequently lowering the ORR energy barrier in consistence with the subsequent theoretical calculations.[31] The spectrum of operando FT-EXAFS and fitting curve are shown in Figure 4b-d and Figures S19 and S20, and the fitting parameters are presented in Table S3. The fitting results show that when the voltage drops from OCP to 0.9 V, La-O coordination appears, and the coordination number of La-O is 1.0 at 0.9 V, which corresponds to the adsorption of *OOH to the La center in La_2-N_6 structure during ORR.[32] When the voltage continues to drop from 0.9V to 0.5V, the oxygen coordination number gradually decreases to ca. 0.5, indicating that *OOH is gradually transformed into *O, or further transformed into *OH. Following the adsorption of oxygenated species, both La-N and La-La bond lengths exhibit significant expansion.[33] This confirms the redistribution of electrons during the ORR process, leading to the reconstruction of the La_2-N_6 structure, which in turn assists in regulating the adsorption behavior of intermediates. Additionally, the coordination numbers of La-N and La-La slightly increase as the potential decreases, suggesting that the La-N and La-La bonds may contribute predominantly to the catalytic activity.[34] WT-EXAFS analysis shows that La_2-NG at different voltages has the maximum signal

at about 4.99 Å^{-1}, which can be corresponding to the La-N/O bond (Figure 4e-h).[35] The second maximum intensity is observed at 6.55 Å^{-1}, which corresponds to the La-La bond, indicating that the La_2-N_6 site was not destroyed and the catalyst structure is very stable during ORR.

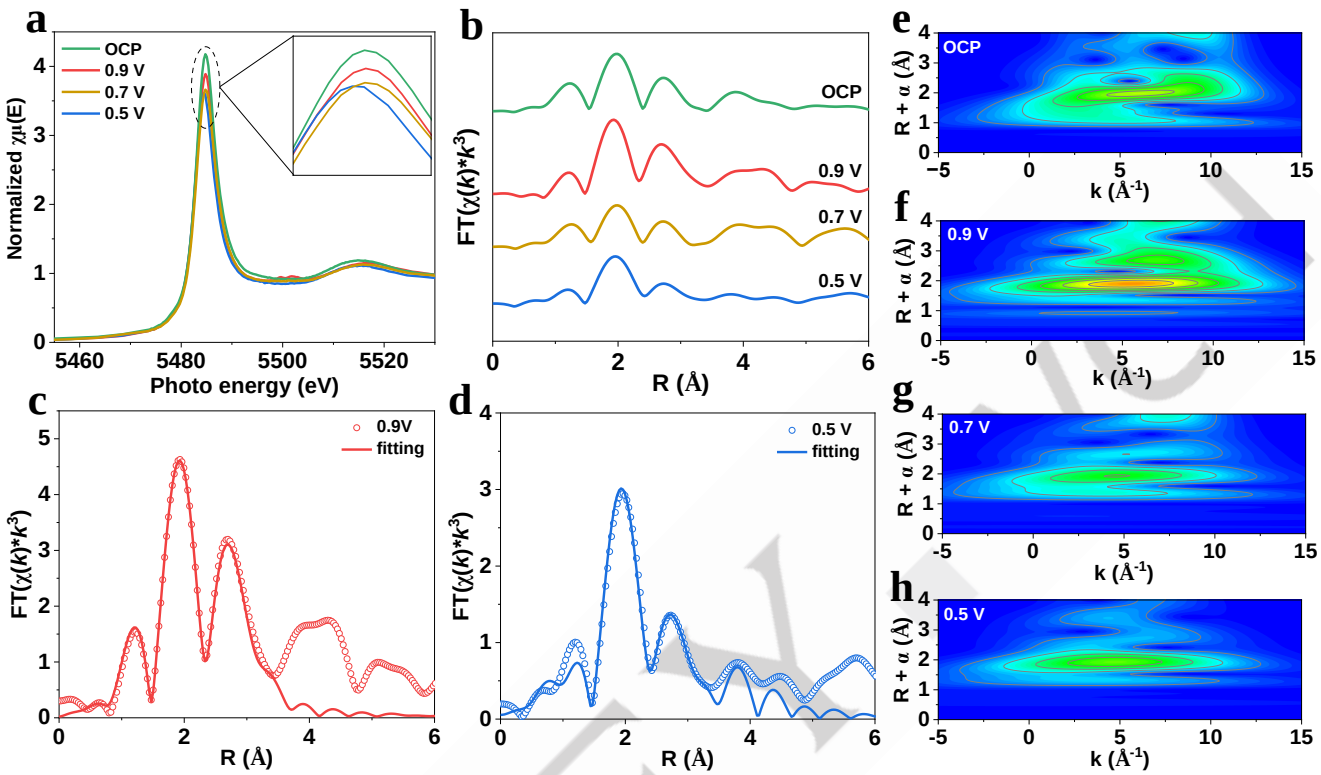

Figure 4. (a) La L-edge XANES spectra and (b) k^3-weighted FT-EXAFS spectra of La_2-NG under different applied potentials during ORR. (c, d) Experiment and FT-EXAFS fitting curve of La L-edge in R space. (e-h) WT-EXAFS spectra of La_2-NG under different applied potentials during ORR.

DFT Calculations

To further investigate the catalytic ORR mechanism on the La_2-NG, we employed DFT calculations to construct five different diatomic La-doped graphene models: dual-atom La doped graphene (La_2-C_x), dual-atom La and N-codoped graphene (La_2-N_6), dual-atom La and N-/O co-doped graphene (La_2-N_2O_4), dual-atom La and O-codoped graphene (La_2-O_6), and single-atom La and N-codoped graphene (La-N_4) as illustrated in Figure 5a and Figures S21-S24. Subsequently, we optimized the adsorption of three ORR intermediates (*OOH, *O, and *OH) on the surfaces of the five models, and determined the ORR pathways on each surface based on the intermediate energy differences (Figure 5b). The results indicate that, across all models, the * → *OOH step is an exothermic process. However, in the subsequent dehydration step to form *O, the surface reaction energy varies significantly among the five models. On the La_2-N_6 surface, a relatively low energy barrier (~0.49 eV) needs be overcome, whereas the La_2-C_x surface exhibits a considerably higher barrier (> 1.10 eV). For other models, this step remains exothermic. In the *O → *OH hydrogenation step, both La_2-N_6 and La_2-C_x require overcoming barriers to proceed, with La_2-C_x presenting a notably high barrier (>2.00 eV). In the final reaction step, the OH → * transition emerges as the rate-determining step (RDS) for all the four dual-atom models, with the La_2-N_6 model showing the lowest reaction barrier (<1.28 eV), whereas all other models display the RDS barrier exceeding 1.90 eV. This critical step significantly impacts the catalytic performance of the dual-atom La-doped graphene catalyst system.

Furthermore, differential charge density maps of the four models reveal that the La_2-N_6 model significantly enhances the charge density on the La dimers due to N coordination, whereas O doping reduces this effect (Figure 5c-f). The projected density-of-states (PDOS) diagrams further show that the conduction and valence bands are well-aligned on the La_2-N_6 surface, promoting efficient charge carrier transfer and facilitating the catalytic activity (Figure 5g-j). In contrast, the La_2-C_x, La_2-N_2O_4, and La_2-O_6 models exhibit minimal overlap between the conduction and valence bands at the Fermi level, indicating lower electron transfer efficiency.

Based on DFT calculations, Bader charge analysis indicates significant differences in charge variations of reaction intermediates on the four models (La_2-C_x, La_2-N_6, La_2-N_2O_4, and La_2-O_6) during the ORR process (Table S4). Notably, the La_2-O_6 model exhibits a marked decrease in the charge on La atoms throughout the reaction, particularly in the *O intermediate structure (Δe^- = −0.24; −0.15). In contrast, the other three models show an overall increase in La atom charge to varying extents. For the La_2-N_6 model, the most pronounced charge

increase occurs when adsorbing the *O intermediate (Δe^- = −0.15; +1.02), whereas in the La_2-C_x and La_2-N_2O_4 models, the greatest charge accumulation on La atoms is observed when adsorbing the *OH intermediate, with changes of −0.07, +0.31 and +0.01, +0.45, respectively. These results suggest that during the ORR process, La atoms tend to gain electrons, resulting in reduced oxidation states in consistence with experimental findings.

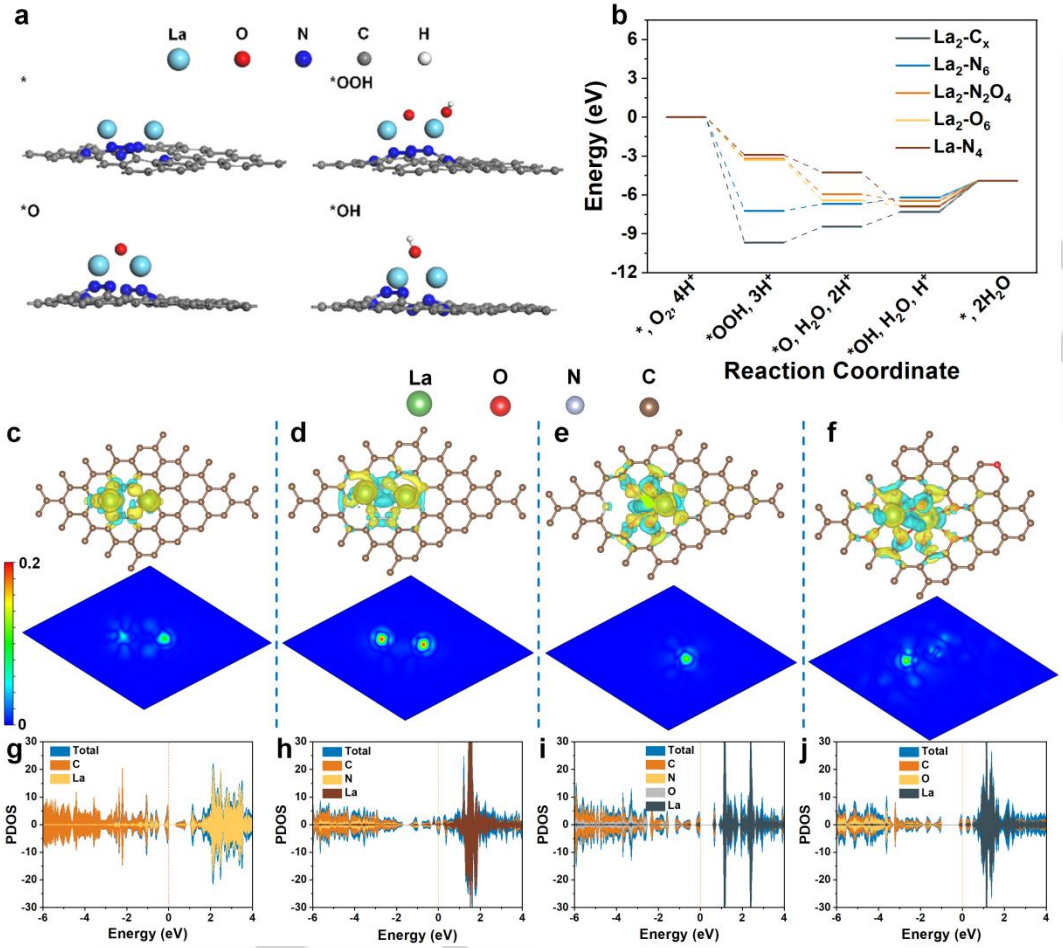

Figure 5. (a) The stable structure of La_2-N_6 model and the intermediate structures for ORR catalytic reaction, * represents the catalyzed surface. (b) Free energy diagram for catalytic reaction. The charge density differences of La_2-C_x (c), La_2-N_6 (d), La_2-N_2O_4 (e), and La_2-O_6 (f). The projected DOS for La_2-C_x (g), La_2-N_6 (h), La_2-N_2O_4 (i), and La_2-O_6 (j).

ZAB Performance Evaluation

Owing to the remarkable ORR electrocatalytic performance of La_2-NG, a ZAB was assembled to explore its application potential (Figure 6a). As illustrated in Figure 6b, the La_2-NG-based ZAB shows an open circuit voltage (OCV) of 1.52 V, which is better than that of the Pt/C+RuO_2-based ZAB (1.46 V). In addition, the best power density and specific capacity of La_2-NG-assembled ZAB are 192 mW cm^{-2} and 805 mAh g_{Zn}^{-1}, respectively, which exceeds those of Pt/C+RuO_2-assembled ZAB (164 mW cm^{-2} and 734 mAh g_{Zn}^{-1}) (Figure 6c, d). The power density and specific capacity of La_2-NG-based ZAB are better than those of most ZABs reported recently (Figure 6e and Table S5). In addition, the discharge voltage of ZABs was measured at intervals of 1 h at different current densities (5 - 50 mA cm^{-2}) (Figure 6f). Pt/C+RuO_2-based ZAB exhibits a large voltage drop, while the discharge voltage of La_2-NG-assembled ZAB decreases more slightly with the increase of discharge current. When the current density returns to 5 mA cm^{-2}, the battery voltage of La_2-NG-based ZAB basically returns to the original voltage. These results demonstrate the good stability and performance maintenance of La_2-NG-assembled ZAB at high current densities. The long-term recyclability of ZABs was evaluated by constant current discharge/charge cycles (Figure 6g and Figure S25). La_2-NG-based ZAB shows stable recyclability after 275 h at 5 mA cm^{-2}, while Pt/C+RuO_2-based ZAB shows significant performance degradation only after 120 h. Specifically, the round-trip efficiency of La_2-NG-assembled ZAB is 60.7% in the first cycle, as shown in Figure 6h. After 275 h of uninterrupted operation, the round-trip efficiency is reduced by only 1.1%, exhibiting excellent reversibility and durability of La_2-NG-assembled ZAB.

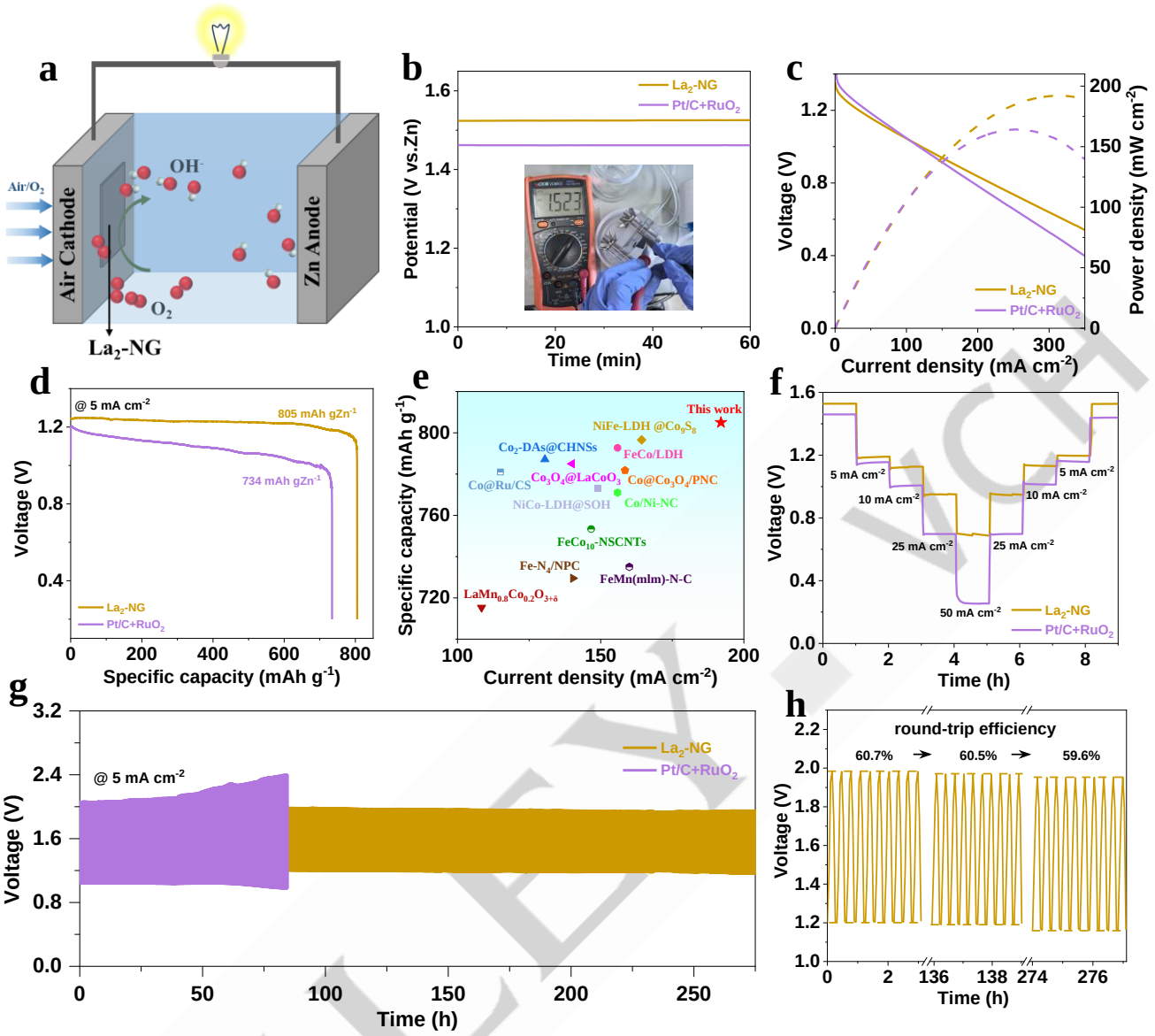

Figure 6. (a) Diagram of ZAB. (b) The OCV diagram of ZABs assembled with La_2-NG and Pt/C+RuO_2. (c) Discharge polarization curve and power density diagram. (d) Specific capacity testing. (e) Comparison of power density and specific capacity for La_2-NG-based ZAB with ZABs assembled with other ORR catalysts. (f) Galvanostatic discharge curves. (g) The charge-discharge curves. (h) Round-trip efficiency of La_2-NG-based ZAB.

Conclusion

In summary, we achieved the preparation of a novel dual-atom La catalyst (La_2-NG) by a Joule ultrafast heating method. The La_2-NG displayed great ORR activity with $E_{1/2}$ of 0.893 V. The ZAB assembled with La_2-NG showed a high OCV of 1.52 V, high power density of 192 mW cm^{-2}, remarkable specific capacity of 805 mAh g_{Zn}^{-1}, and outstanding long-term stability, outperforming those of the ZAB with noble metal Pt/C+RuO_2. Advanced characterizations and DFT simulations revealed that the excellent ORR performance of La_2-NG originates from La_2-N_6 active sites embedded into the graphene skeleton. During the ORR, La_2-N_6 provides a favorable way for the intermediate adsorption, which reduces the reaction barrier of the RDS, thus enhancing the catalytic activity of La_2-NG. Moreover, N coordination significantly increased the charge density on La dimers, promoted the effective charge transfer and enhanced the catalytic process. This study provides an approach for the controllable preparation of rare earth DACs with good ORR activity and stability, and provides a deep understanding about the cooperation mechanism of dual-atom La sites for the ORR.

Supporting Information

The Supporting Information is available free.

Acknowledgements

This work was supported by the National Natural Science Foundation of China (No. 22075099), and the Natural Science Foundation of Jilin Province (No. 20220101051JC). The authors thank BL11B beamline of the Shanghai Synchrotron Radiation Facility (SSRF) for providing the XAFS beamtime.

Keywords: Lanthanum • Dual-atom catalyst • Oxygen reduction reaction • *In situ* XAS • Zn-air battery

[1] a) J. Zhang, M. Yu, S. Tao, *Nano Res.* **2024**, *17*, 7077-7116; b) Y. Gao, L. Liu, Y. Jiang, D. Yu, X. Zheng, J. Wang, J. Liu, D. Luo, Y. Zhang, Z. Shi, X. Wang, Y.-P. Deng, Z. Chen, *Nano-Micro Lett.* **2024**, *16*, 162.

[2] a) X. Han, X. Yu, H. S. Park, *Mater. Chem. Front.* **2024**, *8*, 1536-1562; b) P. Lianos, *Phys. Chem. Chem. Phys.* **2023**, *25*, 11883-11891; c) F. Liu, X. Lu, C. Shi, Z. Sun, *Batteries Supercaps* **2024**, *7*, e202400402.

[3] a) E. V. Rebrov, P.-Z. Gao, *Catalysts* **2023**, *13*, 1289; b) L. Yan, J. Chen, C. Yang, J. Ning, Y. Hu, *Small Sci.* **2023**, *4*, 2300094; c) W. Shao, R. Yan, M. Zhou, L. Ma, C. Roth, T. Ma, S. Cao, C. Cheng, B. Yin, S. Li, *Electrochem. Energy Rev.* **2023**, *6*, 11.

[4] a) Z. Fan, H. Wan, H. Yu, J. Ge, *Chin. J. Catal.* **2023**, *54*, 56-87; b) J. Yu, C. Su, L. Shang, T. Zhang, *ACS Nano* **2023**, *17*, 19514-19525; c) L. Qi, J. Guan, *Sci. Bull.* **2025**, *70*, 1856-1871.

[5] a) J. Hu, W. Liu, C. Xin, J. Guo, X. Cheng, J. Wei, C. Hao, G. Zhang, Y. Shi, *J. Mater. Chem. A* **2021**, *9*, 24803-24829; b) X. Bai, Y. Wang, J. Han, S. Chen, X. Niu, J. Guan, *Chem. Sci.* **2024**, *15*, 19466-19472.

[6] a) A. M. Roth-Zawadzki, A. J. Nielsen, R. E. Tankard, J. Kibsgaard, *ACS Catal.* **2024**, *14*, 1121-1145; b) X. Xu, J. Guan, *Chem. Sci.* **2024**, *15*, 14585-14607; c) S. Ajmal, Y. Zhao, G. Yasin, F. O. Boakye, M. Tabish, M. M. Alam, A. G. Al-Sehemi, W. Zhao, *ChemCatChem* **2024**, *16*, e202301392.

[7] a) L. Peng, L. Shang, T. Zhang, G. I. N. Waterhouse, *Adv. Energy Mater.* **2020**, *10*, 2003018; b) M. Zhou, W. Kong, M. Xue, H. Li, M. A. Khan, B. Liu, F. Lu, X. Zeng, *Catal. Sci. Technol.* **2023**, *13*, 4615-4634.

[8] a) A. Kumar, D. Kumar Das, R. Kishore Sharma, M. Selvaraj, M. A. Assiri, S. Ajmal, G. Zhang, R. K. Gupta, G. Yasin, *Ind. Eng. Chem.* **2023**, *123*, 404-411; b) H. Sakai, S. Hirai, M. Nagao, N. C. Rosero-Navarro, A. Miura, K. Tadanaga, *J. Alloys Compd.* **2023**, *935*, 167986; c) D. Ghosh, S. Parwaiz, P. Mohanty, D. Pradhan, *Dalton Trans.* **2020**, *49*, 17594-17604; d) X. Xu, T. Gan, J. Guan, *CCS Chemistry* **2025**, 10.31635/ccschem.025.202505566.

[9] Y. Wang, J. Wu, S. Tang, J. Yang, C. Ye, J. Chen, Y. Lei, D. Wang, *Angew. Chem. Int. Ed.* **2023**, *62*, e202219191.

[10] X. Wang, Z. Chen, Z. Han, H. Gai, J. Zhou, Y. Wang, P. Cui, J. Ge, W. Xing, X. Zheng, M. Huang, H. Jiang, *Adv. Funct. Mater.* **2022**, *32*, 2111835.

[11] R. Hu, Y. Li, Q. Zeng, J. Shang, *Appl. Surf. Sci.* **2020**, *525*, 146588.

[12] Z. Xiao, P. Sun, Z. Qiao, K. Qiao, H. Xu, S. Wang, D. Cao, *Chem. Eng. J.* **2022**, *446*, 137112.

[13] S. Huang, Z. Qiao, P. Sun, K. Qiao, K. Pei, L. Yang, H. Xu, S. Wang, Y. Huang, Y. Yan, D. Cao, *Appl. Catal., B* **2022**, *317*, 121770.

[14] X. Cheng, Y. Wang, Y. Lu, L. Zheng, S. Sun, H. Li, G. Chen, J. Zhang, *Appl. Catal., B* **2022**, *306*, 121112.

[15] M. Tong, F. Sun, Y. Xie, Y. Wang, Y. Yang, C. Tian, L. Wang, H. Fu, *Angew. Chem. Int. Ed.* **2021**, *60*, 14005-14012.

[16] a) X. Man, Y. Chang, J. Jia, *Mol. Catal.* **2024**, *565*, 114389; b) Z. Chen, X. Su, J. Ding, N. Yang, W. Zuo, Q. He, Z. Wei, Q. Zhang, J. Huang, Y. Zhai, *Appl. Catal., B* **2022**, *308*, 121206; c) L. Li, Y. Li, R. Huang, X. Cao, Y. Wen, *ChemCatChem* **2021**, *13*, 4645-4651.

[17] J. Zhao, J. Liu, C. Jin, N. Wang, F. Wang, *Chem. - Eur. J.* **2020**, *26*, 12606-12614.

[18] L. Yin, S. Zhang, M. Sun, S. Wang, B. Huang, Y. Du, *Adv. Mater.* **2023**, *35*, 2302485.

[19] Y. Zhao, H. Wang, J. Li, Y. Fang, Y. Kang, T. Zhao, C. Zhao, *Adv. Funct. Mater.* **2023**, *33*, 2305268.

[20] a) B. Deng, X. Wang, D. X. Luong, R. A. Carter, Z. Wang, M. B. Tomson, J. M. Tour, *Sci. Adv.* **2022**, *8*, eabm3132; b) W. Chen, J. Chen, K. V. Bets, R. V. Salvatierra, K. M. Wyss, G. Gao, C. H. Choi, B. Deng, X. Wang, J. T. Li, C. Kittrell, N. La, L. Eddy, P. Scotland, Y. Cheng, S. Xu, B. Li, M. B. Tomson, Y. Han, B. I. Yakobson, J. M. Tour, *Sci. Adv.* **2023**, *9*, eadh5131.

[21] J. Jian, Z. Wang, Y. Qiao, M. Wang, P. Nie, L. Chang, *J. Power Sources* **2025**, *629*, 235994.

[22] L. Sun, X. Liu, Y. Feng, X. Ding, J. Wang, N. Jiang, S. Wang, *Appl. Catal., B* **2023**, *338*, 122979.

[23] a) T. Tang, Y. Wang, J. Han, Q. Zhang, X. Bai, X. Niu, Z. Wang, J. Guan, *Chin. J. Catal.* **2023**, *46*, 48-55; b) T. Tang, X. Bai, Z. Wang, J. Guan, *Chem. Sci.* **2024**, *15*, 5082-5112.

[24] L. Yin, M. Sun, S. Zhang, Y. Huang, B. Huang, Y. Du, *Adv. Mater.* **2024**, 10.1002/adma.202416387, 2416387.

[25] M. Liu, X. Wang, S. Cao, X. Lu, W. Li, N. Li, X.-H. Bu, *Adv. Mater.* **2024**, *36*, 2309231.

[26] G. Yang, M. Fan, Q. Liang, X. He, W. Zhang, T. Asefa, *Angew. Chem. Int. Ed.* **2025**, *64*, e202421168.

[27] Z. Zhu, Q. Liu, X. Liu, J. Shui, *J. Phys. Chem. C* **2020**, *124*, 3069-3079.

[28] H. T. Chung, D. A. Cullen, D. Higgins, B. T. Sneed, E. F. Holby, K. L. More, P. Zelenay, *Science* **2017**, *357*, 479-484.

[29] J. Kim, A. A. Gewirth, *J. Phys. Chem. B* **2006**, *110*, 2565-2571.

[30] Z. Weng, L. Liu, Y. Hu, Y. Wei, P. Da, Z. Wu, Z. Mu, P. Xi, C. H. Yan, *Adv. Mater.* **2023**, *36*.

[31] X. Han, T. Zhang, W. Chen, B. Dong, G. Meng, L. Zheng, C. Yang, X. Sun, Z. Zhuang, D. Wang, A. Han, J. Liu, *Adv. Energy Mater.* **2021**, *11*, 2002753.

[32] W. Xu, R. Zeng, M. Rebarchik, A. Posada-Borbón, H. Li, C. J. Pollock, M. Mavrikakis, H. D. Abruña, *J. Am. Chem. Soc.* **2024**, *146*, 2593-2603.

[33] a) X. Zhao, H. Cheng, X. Chen, Q. Zhang, C. Li, J. Xie, N. Marinkovic, L. Ma, J.-C. Zheng, K. Sasaki, *J. Am. Chem. Soc.* **2024**, *146*, 3010-3022; b) Q. Li, D. Zhang, J. Wu, S. Dai, H. Liu, M. Lu, R. Cui, W. Liang, D. Wang, P. Xi, M. Liu, H. Li, L. Huang, *Adv. Mater.* **2023**, *36*, 2309266.

[34] a) X. Liu, Y. Wang, J. Liang, S. Li, S. Zhang, D. Su, Z. Cai, Y. Huang, L. Elbaz, Q. Li, *J. Am. Chem. Soc.* **2024**, *146*, 2033-2042; b) Y. Zhao, H. C. Chen, X. Ma, J. Li, Q. Yuan, P. Zhang, M. Wang, J. Li, M. Li, S. Wang, H. Guo, R. Hu, K. H. Tu, W. Zhu, X. Li, X. Yang, Y. Pan, *Adv. Mater.* **2023**, *36*, 2308243.

[35] S. Ning, M. Li, X. Wang, D. Zhang, B. Zhang, C. Wang, D. Sun, Y. Tang, H. Li, K. Sun, G. Fu, *Angew. Chem. Int. Ed.* **2023**, *62*, e202314565.

10.1002/anie.202509063

Entry for the Table of Contents

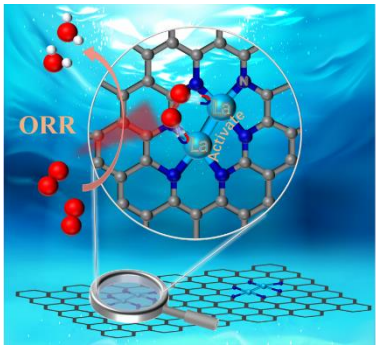

Using an ultra-fast printing technology, we have successfully embedded diatomic lanthanum sites onto graphene framework, which shows excellent ORR performance. La_2-N_6 configuration structure can effectively reduce the reaction barrier of RDS and promote effective charge transfer, thus enhancing the catalytic process, on which the intermediates and structural evolution were well uncovered by combining advanced characterizations and theoretical calculations.